

# The Complete “Z” Track of Circinus X-1

Robert E. Shirey<sup>1,2</sup>, Hale V. Bradt<sup>1</sup>, and Alan M. Levine

*Center for Space Research, Massachusetts Institute of Technology, Cambridge, MA 02139*

**To be published in the May 20, 1999 issue of *The Astrophysical Journal* (Vol. 517)**

## ABSTRACT

We carried out an extensive *Rossi X-ray Timing Explorer* campaign, in 1997 June, to study Circinus X-1 during the active portion of its 16.55-d intensity cycle. The observations spanned 10 days, including 56% coverage for 7 d, and allowed us to find time segments which clearly demonstrate continuous evolution along the horizontal, normal, and flaring branches (HB/NB/FB) of a Z-source low-mass X-ray binary. These results confirm and extend the behavior we inferred from earlier observations. Here we study the continuous evolution of the Fourier power spectra and the energy spectra around the complete hardness-intensity track.

A narrow quasi-periodic oscillation (QPO) peak, previously observed in the power spectra at 1.3–32 Hz, increases in frequency from 12 Hz to 25 Hz moving down a vertical extension of the horizontal branch in the hardness-intensity diagram. These horizontal branch QPOs (HBOs) occur near 30 Hz and fade in strength on the horizontal portion of the HB, while a broad peak in the power spectrum arises near 4 Hz. This peak becomes much more prominent along the normal branch and remains near 4 Hz (the normal branch QPOs, or NBOs). On the flaring branch, neither QPO is present and the power spectrum is dominated by very low frequency noise. We also found that each branch of the spectral track is associated with a specific type of evolution of the energy spectrum. We explored various models for the energy spectrum and parameterized the evolution of the spectrum in terms of a two-component model consisting of a multi-temperature “disk blackbody” and a higher-temperature ( $\sim 2$  keV) blackbody. We also show that an unusual line- or edge-like feature occurs at about 10 keV in energy spectra from the flaring branch and lower normal branch. This unusual feature is very similar to one seen on the FB and lower NB of the Z source GX 5–1.

*Subject headings:* Stars:individual(Cir X-1) — stars:neutron — X-rays:stars

---

<sup>1</sup>Department of Physics, Massachusetts Institute of Technology, Cambridge, MA 02139

<sup>2</sup> Present address: Department of Physics, University of California, Santa Barbara, Santa Barbara, CA 93106; shirey@orion.physics.ucsb.edu

## 1. Introduction

Circinus X-1 exhibits a dramatic 16.55-d cycle of X-ray flaring which is believed to be the result of enhanced mass transfer occurring near periastron of a highly eccentric binary orbit (Kaluzienski et al. 1976; Murdin et al. 1980). Although the identification of the orbital period seems to be secure, there is very little direct evidence concerning the masses of the two components of the binary and the other orbital parameters. Nonetheless, the compact component is thought to be a weakly magnetized neutron star on the basis of three type I X-ray bursts seen with *EXOSAT* (Tennant et al. 1986). Further type I bursts have not been observed from Cir X-1 since the *EXOSAT* discovery, possibly because the source intensity has been higher during subsequent observations. No coherent pulsations, which would be expected to be present if the compact star is a strongly magnetized neutron star, have been detected (Dower, Bradt, & Morgan 1982; Vaughan et al. 1994).

Quasi-periodic oscillations (QPOs) were seen at 1.4 Hz, 5–20 Hz, and 100–200 Hz in *EXOSAT* observations of Cir X-1 in a bright state (Tennant 1987; Tennant 1988), but other observations at lower intensity showed no such QPOs (Oosterbroek et al. 1995). Based on these data, it was suggested that Cir X-1 is an atoll-source low-mass X-ray binary (LMXB) that can uniquely reach the Eddington accretion rate and exhibit normal/flaring branch QPOs (NBOs/FBOs) at 5–20 Hz (Oosterbroek et al. 1995; van der Klis 1994). Similar QPOs were observed in *Ginga* observations of Cir X-1 (Makino 1993).

Observations with the All-Sky Monitor (ASM) and Proportional Counter Array (PCA) on the *Rossi X-ray Timing Explorer* (*RXTE*) have shown that since early 1996 (from the beginning of *RXTE* monitoring) the baseline intensity level of Cir X-1 has remained bright ( $\sim 1$  Crab, 2–12 keV;  $\sim 1060 \mu\text{Jy}$  at 5.2 keV) at all phases of the 16.55-d cycle, with both dips and flares associated with phase zero of the cycle (Shirey et al. 1996, 1998, hereafter Papers I & II; Shirey 1998). During non-flaring phases (intensity  $\approx 1$  Crab) of a cycle in 1996 March, the centroid frequency of a narrow QPO was observed to evolve between 1.3 Hz and 12 Hz and was strongly correlated with the cutoff frequency of low-frequency noise and with the centroid frequency of a broad peak ranging from 20–100 Hz, at  $\sim 13$  times the frequency of the lower frequency QPO (Paper I). During portions of a

more active cycle in 1997 February–March, a similar narrow QPO evolved between 6.8–32 Hz, while during other portions of the cycle, a broad QPO was observed at 4 Hz (Paper II). By correlating the timing properties with fragmented branches in hardness-intensity diagrams, we identified horizontal, normal, and flaring branches. Thus, we interpreted the narrow 1.3–32 Hz QPOs in Cir X-1, including the 5–20 Hz QPOs observed with *EXOSAT*, as horizontal-branch oscillations (HBOs), and the broad 4 Hz QPOs as NBOs, thus calling into question the earlier interpretation of the QPOs in Cir X-1.

In this paper we present results from a 10-day set of high-efficiency *RXTE* observations, including 56% coverage for 7 d starting 1.5 d before phase zero. Portions of these data show a complete Z-source track for Cir X-1. These results confirm our previous interpretation based on incomplete and shifted spectral tracks constructed from shorter and more widely spaced observations. We show how both the Fourier power spectra and the energy spectra evolve along the various spectral tracks. We explore possible models for the energy spectrum and parameterize the evolution by fitting the data at various points along the hardness-intensity track to a model consisting of a multi-temperature “disk blackbody” and a higher-temperature isothermal blackbody.

## 2. Observations

The PCA light curves and a hardness ratio (“broad color”) for the 1997 June observations are shown in Figure 1. These data show only moderate variability for the first day of observations. The source entered a phase of significant dipping during the half day before phase zero (day 611.5), based on the radio ephemeris (Stewart et al. 1991). The hardness ratio shows that dramatic spectral evolution, both hardening and softening, occurs during these dips.

By phase zero the main dipping episode ends, and the transition to the flaring state begins. While the intensity increases by more than a factor of three in the lowest energy band (2–6.3 keV), the intensity between 6.3 keV and 13 keV does not climb at all, and above 13 keV it decreases by a factor of about 10 over the first 1.5 days following phase zero. This anti-correlation of the low and high-energy intensity during the transition results in a decreased hardness ratio after phase zero, as is observed in *RXTE* ASM data (Papers I & II; Shirey 1998).

After a relatively smooth transition toward high total intensity (2–18 keV) during the first day following phase zero, the intensity becomes highly variable (i.e., the “active” or “flaring” state) for the remaining 7 days of the observation. The intensity in the hard band remains much lower than before phase zero but shows strong variability with a peak value that gradually increases from about 24 to 36 counts s<sup>-1</sup> PCU<sup>-1</sup>. Based on the results in Paper II and those discussed below, we can identify short-term variability within restricted limits as motion along branches in hardness-intensity diagrams and the gradual evolution of the limits as shifting of the branches.

### 3. Complete Track in Hardness-intensity and Color-color Diagrams

The color-color and hardness-intensity diagrams (CDs/HIDs) for all data in Figure 1 are shown in Figure 2. Only data from three of the five PCA detectors, PCUs 0, 1, and 2, were included in the diagrams, since PCUs 3 and 4 were not operating during portions of the observations. These data cover a significant portion (10 d) of an entire 16.55 d cycle. Data from before day 612.5 generally had soft color  $\gtrsim 1.5$  and broad color  $\gtrsim 0.325$ , while the data after day 612.5 generally fell below those values.

The dips seen in Figure 1 appear as prominent but less dense tracks with two sharp bends in the CD (initially toward the right of the main arc-shaped locus) and one sharp bend in the HID ( $I < 2.3$  kcounts s<sup>-1</sup> PCU<sup>-1</sup>). We show in another paper (Shirey, Levine, & Bradt 1999) that tracks with these shapes are due to a variably absorbed bright spectral component plus an unobscured faint component. Brandt et al. (1996) used a similar model to explain the spectral changes during an intensity transition of Cir X-1 observed with *ASCA*. Having identified absorption dip signatures, we now focus on non-dip spectral behavior, which is presumably more directly related to the mechanisms of X-ray production.

Most of the data in Figure 2 fall along a single arc-shaped locus in the CD and a more complicated structure in the HID. We use spectral bands with lower energies than those used for the 1997 February–March observations in Paper II; this enhances the branch structure in the CD. When the diagrams for the two observations are constructed in the same manner, with the same hardness ratios and only three PCUs rather than five, the data from these two cycles cover

approximately the same extent in both diagrams. The high-efficiency coverage of the current observations resulted in tracks that are more complete than the tracks of the earlier observations. Unpublished data from several other cycles observed with the PCA also fall in similar regions of the diagrams as the data in Figure 2.

The detailed structure within the overall locus of CD/HID points is revealed in CD/HID plots of data divided into shorter time segments ( $\lesssim 12$  h). In particular, four time segments labelled “A”, “B”, “C”, and “D” in Figure 1 have been selected for further study. The intensity from time segments A and B (days 609.93–610.16 and 610.66–610.90 respectively) shows minimal variability in each energy channel, and thus these time segments produce small CD/HID clusters whose locations are indicated in Figure 2. The source was more active during time segments C and D (days 612.625–613.125 and 616.075–616.600 respectively), and the CD/HID tracks from these times show several connected branches. Enlarged views of the CD and HID for these time segments are shown in Figure 3. The full ranges of the diagrams of Figure 3 are indicated by dashed rectangular boxes in Figure 2. Tracks of other time segments generally each resemble some portion of the entire pattern shown in Figure 3, but often with a shifted position in the diagrams.

The data from segment C in Figure 3 include some absorption dips, which result in tracks moving off the right side of the CD and the left side of the HID (and far beyond the limits of the plot in both cases). The timing and spectral data associated with these absorption dips will be omitted from analysis of the HID branches.

The HID patterns reveal the shape of the full “Z” track as previously inferred from the fragmented tracks in Paper II. Time segments C and D both show a horizontal branch, a normal branch, and a flaring branch which turns above the normal branch. In addition, segment C exhibits a long nearly-vertical extension on the left end of the HB, while for segment D, there is only a small hint of an upward turn at the left end of the HB. The HIDs show significant shifts of the HB and upper NB between the time segments C and D, which were separated by several days.

The branches in the CDs of Figure 3 are less well-separated than those in the HIDs. This was also the case for the diagrams in Paper II. However, the flaring branch clearly turns above the normal branch in

the lower left part of the current CDs, and the upturned left extension of the HID horizontal branch of segment C is marked by an increase in the slope in the upper right part of the associated CD.

The HID for segment C is similar to that derived from *RXTE* PCA observations of the Z source Cyg X-2 (Smale 1998). The Cyg X-2 HID also shows a very prominent vertical extension of the HB. A similar upturned HB was reported in *Ginga* and *EXOSAT* observations of GX 5–1 (Lewin et al. 1992; Kuulkers et al. 1994). The upturned flaring branch is similar to the flaring branch observed in the CD for the Z source GX 349+2 in recent *RXTE* PCA observations (Zhang et al. 1998).

The HID track for time segment C was divided into 20 regions which were used to group data for further timing and spectral analysis. The 20 regions have been numbered as shown in Figure 4, with numbers increasing from the vertical HB, through the NB, to the FB. We show below that region 6 does not adhere to the otherwise monotonic variation of spectral/temporal characteristics with region number. This region may be an indication of an upward-shifted horizontal portion of the HB.

Details of the temporal variability of the intensity, hardness ratio, and HID region numbers for time segment C are shown in Figure 5. During this half-day segment, the source generally moves from lower to higher region number as the observation progresses. Thus, the time series can be divided into four sub-segments which predominantly correspond to each portion of the HID track: the vertical and horizontal portions of the HB, the NB, and the FB. Absorption dips occur in all but the flaring branch during this particular data set; these are easily identified by brief intensity dips coupled with pronounced increases in broad color. No region number was assigned to most data points from dips since the HID regions in Figure 4 were selected to avoid dips.

The light curves of the different branches (Fig. 5) exhibit the following characteristics, excluding the behavior associated with the dips. When the source is on the vertical portion of the HB, the intensity evolves relatively smoothly, with a slight increase in the 2–6.3 keV band and a decrease of almost a factor of two in the 13–18 keV band. On the horizontal portion of the HB, the source shows a substantial increase in soft intensity and on average shows relatively steady hard intensity. On the normal branch, the intensity is high in the soft band while decreasing and highly

variable in the hard band. The NB/FB transition occurs at lower intensity in all bands compared to most of the NB. The flaring branch itself is then produced by high-variability “mini-flares” or bursts above the NB/FB apex level (region 17).

Although the HID regions were defined such that obvious absorption tracks were avoided, one brief dip, at day 612.98, occurred from region 12 on the normal branch and placed a few points artificially across regions 9, 7, and 5. These points are easily identified in Figure 5 (bottom plot) and are thus not included in subsequent timing and spectral analysis.

Likewise, the highest mini-flares on the flaring branch actually extend beyond region 20 and cross regions 8 and 9. In fact a few such points can even be seen above region 10 in Figure 4. The FB points that fell into HB regions can also be clearly identified as points with region numbers of 8 or 9 in the FB portion of Figure 5. These are not included in subsequent timing and spectral analysis.

#### 4. Evolution of the Power Density Spectrum

Fourier power density spectra (PDSs) were computed for each 16 s of time segment C. Each transform used  $2^{16}$  244- $\mu$ s ( $2^{-12}$  s) time bins and covered the full 2–32 keV energy range. The expected Poisson level, i.e., the level of white noise due to counting statistics, was estimated taking into account the effects of deadtime (Morgan et al. 1997; Zhang et al. 1995; Zhang et al. 1996) and subtracted from each PDS; this method tends to slightly underestimate the actual Poisson level. For each of the 20 HID regions defined in Figure 4, an average PDS was calculated from the power spectra corresponding to points in that region. The average PDSs were then logarithmically rebinned and are shown in Figure 6.

The general features of the power spectra are similar to those observed in previous PCA observations (see Papers I & II). In Paper II, based on features of the power spectra associated with fragmented spectral tracks, we identified many of these features with those of a Z-source, and we discussed the properties of the QPOs on the horizontal and normal branches. In the current observations, the characteristics of the time variability are seen to evolve smoothly during a single 12-h observation (segment C). The narrow QPO is observed to evolve from 12 Hz in region 1 to 25 Hz in region 7 as the HID location moves down the vertical extension of the HB (region 6 may be a

shifted version of 8). Across the horizontal portion of the HB (regions 8–11), the narrow QPO fades into a knee close to 30 Hz, while the broad QPO gradually rises near 4 Hz. The broad QPO is present near 4 Hz along the normal branch (regions 12–16). It is most prominently peaked in the middle of the branch and weak at the bottom of the branch (region 17). On the flaring branch (regions 18–20), no QPOs are present and the power spectrum shows only strong very low frequency noise.

The PDS properties of the horizontal portion of the HB are somewhat similar to those of the upper normal branch of some Z sources, namely no significant evolution of the HBO frequency and weak NBOs. However, we will continue to refer to this branch as part of the the HB since other Z sources also show both vertical and horizontal portions of the HB (see above).

## 5. Evolution of the Energy Spectrum

The Standard2 data mode of the PCA instrument produces 129-channel energy spectra every 16 s. A parallel background file was constructed using the “pcabackest” program<sup>1</sup> provided with the FTOOLS analysis package (version 4.0). Average pulse-height spectra (and background spectra) were constructed for each of the 20 HID regions, separately for each of the five PCUs. Version 2.2.1 response matrices were used in the analysis of these spectra. A 1% systematic error estimate was added in quadrature to the estimated statistical error ( $1\sigma$ ) for each channel of the spectra to account for calibration uncertainties. Although the instrument response matrix is imperfectly known, we can safely assume that any spectral features that vary during the 12-hours spanned by time segment C are due to evolution of the source spectrum. Representative spectra from the hard, bright, and soft extremes (regions 1, 11, and 17, respectively) of the evolution along the HID track are shown in Figure 7.

The evolution of the spectrum may be studied by inter-comparison of ratios of pulse-height spectra from each region to that of a reference spectrum, from region 11 (Fig. 8). The spectrum is hardest in region 1, at the top of the vertical extension of the hor-

izontal branch. Motion down the branch (softening, regions 1–7) corresponds to pivoting of the spectrum about  $\sim 7$  keV, i.e., increasing intensity below  $\sim 7$  keV and decreasing intensity above that energy. Motion to the right across the horizontal portion of the HB (regions 8–11) corresponds to continued increasing low-energy intensity with modest softening, but with a nearly constant spectrum above 12 keV. Note that in the hardness ratios of Figure 4 the high-energy channel (6.3–13 keV) is dominated by photons near the lower bound of the interval.

When the source moves down the normal branch (regions 11–17), the flux generally decreases across the entire 2.5–25 keV band but decreases most significantly at high energy from region 11 to 15 (thus further softening). Moving down the NB, the spectrum gradually develops a dip or step above  $\sim 9$  keV and a peak slightly above 10 keV. Motion up the FB (regions 18–20) is produced by increasing intensity at intermediate energies with a relatively constant spectrum at low energy, thus hardening. The peaked feature near 10 keV becomes more prominent moving up the FB and will be discussed below.

## 6. Selection of Spectral Models

Spectral forms (e.g., blackbody emission, a power law, etc.) for use in fitting the spectra from the HID regions were explored by first applying them to high-quality spectra from time segments A and B (see Fig. 1). Variability in both of these segments was limited to less than 10% in all energy bands between 2.5–18 keV. We thus constructed a single (averaged) pulse-height spectrum, known hereafter as spectrum A or spectrum B, for the entire 17–19 ks of each segment. Errors in these spectra are dominated by the 1% systematics at all energies up to  $\sim 20$  keV.

The timing properties measured throughout data sets A and B indicate that time segment A falls on the vertical portion of the HB (strong narrow QPO at 8.4–11.5 Hz) and time segment B falls near the HB/NB apex (weak narrow QPO above 30 Hz and/or the broad 4 Hz QPO). The locations of time segments A and B in Figure 2 indicate that the branches are significantly shifted relative to those of segments C and D.

Remillard et al. (1998) studied version 2.2.1 PCA response matrices using Crab nebula data and found that the response model was most accurate for PCUs 0, 1, and 4 (of the five PCA detectors) and for energies

<sup>1</sup>The background model was defined in three files provided by the PCA instrument team at NASA/GSFC: `pca_bkgd_q6_e03v01.mdl`, `pca_bkgd_xray_e03v02.mdl`, and `pca_bkgd_activ_e03v03.mdl`.

between 2.5 keV and 25 keV. Thus, in fitting spectra we only include data from PCUs 0, 1, and 4 and from energy channels corresponding to 2.5–25 keV. Spectra from each of these detectors are fit separately. Fit parameters reported are the average values for PCUs 0, 1, and, when appropriate, 4. Errors are conservatively estimated as the entire range encompassed by the 90% confidence intervals from each of the detectors. PCU 4 consistently gives lower normalizations for fitted spectral components, so fit parameters from that detector are not included when computing the average normalizations and flux values and their errors. Spectrum B was not constructed for PCU 4 since that detector was turned off during part of time segment B.

Interstellar photoelectric absorption was included in all models. The absorption model used solar abundances (Anders & Ebihara 1982) and cross-sections given by Morrison & McCammon (1983).

Several single-component models were fit to spectra A and B. Blackbody and power-law models fit very poorly in both cases, as did a multi-temperature “disk blackbody” spectrum (Mitsuda et al. 1984; Makishima et al. 1986; model “diskbb” in XSPEC), with reduced  $\chi^2$  ( $\chi_r^2$ ) values of 22–545. A thermal bremsstrahlung model provided a better fit to spectrum B ( $\chi_r^2 = 4.0$ ), but fit spectrum A poorly ( $\chi_r^2 = 34$ ). A relatively good fit was achieved for both spectra with a modified bremsstrahlung model (see Table 1) which includes the effects of Compton scattering of bremsstrahlung photons to higher energy in an optically thick plasma cloud (Lamb & Sanford 1979; model “compLS” in XSPEC).

A number of two-component models were also fit to these two spectra. A model using a disk blackbody and power law did not fit well ( $\chi_r^2=3-5$ ), mainly because a single power-law slope does not adequately describe the spectrum at high energy. A blackbody with  $kT \gtrsim 2$  keV is often included in models of the hard X-ray emission of LMXBs thought to contain a neutron star, where emission from or near the surface might produce high-temperature blackbody emission with a small effective area. Two blackbodies ( $kT \sim 1.1$  keV and 2.2 keV) fit moderately well (see Table 1), but required negligible interstellar absorption. The low absorption is inconsistent with previous measurements from *ASCA* and *ROSAT* (both sensitive below 2 keV where the absorption is most easily constrained) which were used to estimate the interstellar column density to be  $N_H = (1.8-2.4) \times 10^{22} \text{ cm}^{-2}$

(Brandt et al. 1996; Predehl & Schmitt 1995).

Two models commonly used to fit Z-source energy spectra are the “Western model” and the “Eastern model” (Hasinger et al. 1990; Asai et al. 1994). The Western model consists of blackbody emission from the hot surface of the neutron star or from a boundary between the accretion disk and surface, plus a Boltzmann-Wien component due to unsaturated Comptonization of soft photons by hot electrons (White et al. 1986; Schulz, Hasinger, & Trümper 1989; Langmeier, Hasinger, & Trümper 1990; Schulz & Wijers 1993). The Eastern model also includes blackbody radiation emitted from or near the surface, plus emission from a multi-temperature accretion disk (Mitsuda et al. 1984; Hoshi & Mitsuda 1991; Hirano et al. 1995).

The Western model, a power law with a high-energy exponential cutoff plus a blackbody, fit well (see Table 1), but the best-fitting high-energy cutoff energy ( $E_{cut} \approx 1.7$  keV) was so low relative to the PCA bandpass ( $\gtrsim 2$  keV) that the power law photon index was not well constrained. The Eastern model, a disk blackbody with temperatures at the inner edge of the disk of 1.5–1.8 keV, plus a  $\sim 2$  keV blackbody, fit spectra A & B quite well (see Table 1 and Fig. 9) and gave absorption column densities roughly consistent with the *ASCA* and *ROSAT* values. Although a number of other two-component models also produce similar quality fits, the Eastern model is used below to provide a physically motivated parameterization of the spectra from the HID regions.

The Eastern model fit to spectrum A (Fig. 9) shows peaked residuals at 6–7 keV, suggesting the presence of an emission line, probably iron  $K\alpha$ . Very similar residuals appear in most of the fits discussed above for both spectra A and B. Addition of a Gaussian line to the models does in fact improve the fits in almost all cases; however, the best-fitting line often has an extremely large Gaussian width ( $\sigma > 1$  keV). The energy resolution of the PCA is about 1 keV FWHM at 6 keV; thus it is difficult to place reliable constraints on parameters such as the centroid and width of a narrow component. We have not included an emission line in the fits reported in Table 1. The presence of an emission line near 6.4 keV is discussed in more detail in Shirey et al. (1999) in conjunction with spectra of absorption dips, which show the line more prominently.

## 7. Fits to Spectra from 20 HID Regions

A disk blackbody plus isothermal blackbody model was fit to the average spectrum for each of the 20 HID regions. Representative fits and residuals are shown in Figure 10. The resulting fit parameters are listed in Table 2 and plotted versus HID region number in Figure 11. The distance to Cir X-1 has been estimated to be about 6–10 kpc (Stewart et al. 1991; Goss & Mebold 1977), so we adopt a value of 8 kpc in converting blackbody and disk blackbody normalizations to radii.

Although both spectra A and B are fit well by the Eastern model, the reduced chi-squared values in Table 2 indicate that none of the fits for the 20 regional spectra are formally acceptable. The fit results must therefore be regarded as an approximate description of the spectrum and its evolution. We emphasize that here, as in any case, caution is advised in drawing physical conclusions from the best-fit model parameters.

The spectra along the horizontal branch (regions 1–11) were all fit relatively well. The residuals for these fits (see Fig. 10) are similar in structure to those for spectra A and B above. Thus they also suggest the presence of an emission line from iron. These spectra all show column densities of  $1.8\text{--}2.3 \times 10^{22} \text{ cm}^{-2}$ , consistent with the *ASCA* and *ROSAT* values discussed above. The temperature of the  $\sim 2.0$  keV blackbody is relatively stable on the HB (see Fig. 11). The temperature of the inner disk decreases from region 1 to region 5 (down the vertical portion of the branch) and then stabilizes at  $\sim 1.3$  keV. The cooling is at least in part responsible for the pivoting of the spectrum on the vertical portion of the HB.

The inner radius of the disk blackbody component, times a factor of order unity involving the inclination angle of the disk, increases from 19 to 33 km, while the radius of the blackbody remains between 3 and 4 km. These size scales are consistent with the hypothesis that these components arise from emission close to a neutron star. In this model, an increasing inner radius of the accretion disk is the most significant factor in producing the HB track; however, one should use caution in interpreting this as an actual physical radius. The inclination angle of the disk in Cir X-1 is unknown but might be high since absorption dips are observed.

From region 1 to 11, the total 2.5–25 keV flux increases monotonically, with the exception of region 6,

from  $2.89 \times 10^{-8}$  to  $4.35 \times 10^{-8} \text{ erg cm}^{-2} \text{ s}^{-1}$ , corresponding to 1.2–1.8 times the Eddington luminosity limit for a  $1.4 M_{\odot}$  neutron star at 8 kpc.

Along the normal branch, the quality of the fits decrease from region 12 to region 17, as indicated by increasing  $\chi_r^2$  values (see Table 2). The absorption column density gradually decreases by a factor of two, but this may be related to the decreasing fit quality. The inner radius and temperature of the disk blackbody change only slightly on the normal branch. In contrast, the  $\sim 2$  keV blackbody begins to fade on the upper portion of the normal branch (regions 12–14), as indicated by a decreasing radius for the emission area. The fading blackbody is illustrated in Figure 12, which shows the modeled incident spectra and both model components for several spectral fits. By the middle of the normal branch, the  $\sim 2$  keV blackbody has faded entirely and fits have lower  $\chi_r^2$  values without it. Thus, the blackbody is omitted from the fits for regions 15–20. The residuals below  $\sim 6$  keV continue to appear similar to those on the HB (see Fig. 10). The peak at  $\sim 6.5$  keV becomes broader and more complicated than on the HB, and the dip and peak above 8 keV become more prominent.

On the flaring branch (regions 18–20), the fit quality decreases further, accompanied by very low values for the absorption column density. A number of other spectral models were fit to the HID-region spectra, and all failed to satisfactorily fit the spectra from the lower portion of the HID track (region number 14 and greater). A significant contribution to the high  $\chi^2$  values on the flaring branch is due to the feature near 10 keV. Addition of a Gaussian line or an absorption edge at 9–11 keV does improve the fits somewhat, but these components cannot account for all the residuals near that energy. A combination of a line *and* an edge near 10 keV can adequately fit the residuals, but such features are difficult to justify physically at that energy. Even hydrogen-like iron can be ruled out as a possible cause due to the high energy of the feature. Many X-ray pulsars show cyclotron absorption features at high energy. Inclusion of a cyclotron absorption component in the spectral model results in a fit similar in quality to that of an absorption edge. However, such features require magnetic fields of  $\sim 10^{12}$  G, which would be expected to result in strong pulsations rather than Z or atoll behavior.

## 8. Discussion

Our spectral and timing analysis of the current observations shows clear evidence for Z source behavior in Cir X-1. This is significant because Cir X-1 was reported to exhibit atoll source behavior at lower intensity (Oosterbroek et al. 1995). Earlier *RXTE* observations, each lasting about two hours and separated by about two days, showed fragments of one or two spectral branches in hardness-intensity diagrams (Paper II). In the much more extensive observations presented in this paper, we have found longer 12-hour segments (time intervals C and D) which clearly exhibit all three branches of a Z source. We have demonstrated that these complete Z tracks shift in the HID, confirming the behavior we inferred from the fragmented tracks of the previous observations.

The current data also allow us to demonstrate how the timing properties evolve along the complete HID track of Cir X-1 and confirm our original identification, in Paper II, of horizontal and normal branch QPOs. Fourier power spectra for different regions of the complete HID track show continuous evolution from the narrow QPO (increasing in frequency from 12 Hz to 30 Hz in the current observations) on the horizontal branch, to the broad 4 Hz QPO on the normal branch, to only very low frequency noise on the flaring branch. Properties of the fast timing characteristics associated with spectral branches in Cir X-1 were discussed in Paper II. For the remainder of this discussion we focus on the properties of the energy spectrum.

We tried fitting energy spectra of Cir X-1 with various simple models. The spectra for time intervals A and B were well fit using the Western and Eastern models (see discussion below), but no simple spectral form was found that fit the range of spectra seen during time interval C. We have not attempted to go beyond simple parameterized spectral models, e.g., by computing model spectra based on the "unified model" of Lamb and collaborators (Lamb 1989; Psaltis, Lamb, & Miller 1995; Psaltis et al. 1998), which was proposed to explain the X-ray spectra and rapid variability of Z sources. Such sophisticated models may be necessary to correctly interpret the spectral changes in Cir X-1 and other Z sources.

The fits of spectra A and B with the Western model yielded a cutoff energy of  $\sim 1.7$  keV for the Comptonized (Boltzmann-Wien) component. The cutoff energy in GX 5-1 was found to be 1–3 keV (Asai

et al. 1994), similar to our results for Cir X-1, but was found to be higher, 4–6 keV, in Cyg X-2 (Hasinger et al. 1990). We did not use the Western model in parameterizing evolution associated with the "Z" track because the cutoff energy in Cir X-1 is low relative to the PCA bandpass, resulting in a poorly constrained power law index and absorption column density.

Parameters for the Eastern model were more well-constrained (see Table 1), and thus this model was used to parameterize the spectral variations associated with the hardness-intensity track. In this model, motion along the HB is mainly associated with an increasing inner radius of the disk (increasing disk blackbody normalization) but also by a decreasing inner disk temperature. This would imply that, as the luminosity increases across the HB, the inner edge of the disk is pushed further away from the surface. It is not clear how this is related to the increasing QPO frequency, which would typically be expected to require a *decreasing* radius if the QPOs were related to Keplerian motion at the inner edge of the disk, e.g., through the magnetospheric beat frequency model (Alpar & Shaham 1985; Lamb et al. 1985).

Fits of the Eastern model to energy spectra from the normal branch indicate that the  $\sim 2$  keV blackbody gradually fades away, leaving only the disk blackbody. This is similar to the result obtained when the Eastern model was fit to the spectrum of Cyg X-2, where the blackbody luminosity decreases from the HB to the FB (Hasinger et al. 1990). Furthermore, the FB of GX 5-1 is characterized by intensity dips which in the Eastern model can be explained by disappearance of the blackbody component, suggesting that accretion flow onto the neutron-star surface is interrupted (Mitsuda et al. 1984).

On the lower NB, a feature in the spectrum develops above 10 keV. This feature becomes more prominent on the flaring branch. A very similar line-like feature at  $\sim 10$  keV was reported in *Ginga* observations of the Z source GX 5-1 (Asai et al. 1994). In GX 5-1, as in Cir X-1, the feature was present on the lower NB and stronger on the FB; we thus suggest that these features of the two sources may be of similar origin. Asai et al. showed that a peak near 11 keV occurs in the correlation coefficients of the time-series data of different energy bands versus the 1.7–4.0 keV band. This demonstrates a temporal character in the narrow band at 11 keV different than that at adjacent energies. In turn, this gives assurance that the line-like feature at that energy is



not the result of the continuum model used to fit the spectrum but is intrinsic to the source. We carried out similar cross-correlation analysis for each of the 20 HID regions in our study. The cross-correlation results, relative to the 2.5–2.9 keV band, from three representative regions are shown in Figure 13. We find a clear peak in the cross-correlation coefficient at about 11 keV in regions 19 and 20 of the FB, further confirming the similarity of the spectral features in Cir X-1 and GX 5–1. Regions 16 and 17 of the lower NB show an abrupt drop in the cross-correlation coefficient above 8–10 keV. The cross-correlation coefficients on the HB and upper NB, where the line- or edge-like 10 keV spectral feature is absent or weak, generally show much less remarkable behavior.

Asai et al. found that that the spectral feature near 10 keV in GX 5–1 was better fit with a Gaussian line rather than, e.g., an absorption edge. However, as we mentioned above, such a feature cannot be produced by even hydrogen-like iron. Asai et al. discuss several of the mechanisms that could possibly produce a line at  $\sim 10$  keV. For example, emission from a heavy element such as Ni could produce the line, but is unlikely since iron should be far more abundant than the heavier elements. Alternately, a line could be blue-shifted due to motion in a relativistic jet or rotation in the accretion disk, but extreme conditions would be required to boost the energy up to  $\sim 10$  keV and one might expect a red-shifted line to also be observed in the X-ray spectrum. As mentioned above, we find that in Cir X-1 an emission line component alone is insufficient to produce the observed structure of the feature. Both line-like and edge-like components may be required to explain this unusual spectral feature at high energy.

Cir X-1 exhibits a number of unusual features in its Z-source behavior in addition to the 10 keV spectral feature. Its HBOs are observed at frequencies as low as 1.3 Hz (Paper I), an order of magnitude lower than those of other Z sources. The highest frequency reached by HBOs in Cir X-1, at the HB/NB apex, is 30–32 Hz (Paper II), about a factor of two below the extreme HBO frequency in other Z sources. Power spectra of Cir X-1 show a broad high-frequency peak, centered at 20–200 Hz, which shifts in frequency maintaining an almost constant ratio with the HBO frequency (Paper I; Tennant 1987). Cir X-1 shows a long vertical extension of the HB. The entire HID track shows very large color/intensity shifts, possibly associated with the presumed eccentric 16.55-d

binary orbit (Paper II). Atoll behavior has been reported at lower intensity (Oosterbroek et al. 1995). It is likely that some or many of these unusual features are related by some physical property of the system, indicating that Cir X-1 may provide important constraints on models of low-mass X-ray binaries.

We would like to acknowledge the *RXTE* teams at MIT and GSFC for their support. In particular we thank E. Morgan, R. Remillard, W. Cui, and D. Chakrabarty for useful discussions related to this work. We thank D. Psaltis for useful discussions regarding Z-source spectral models. We also appreciate the detailed comments and suggestions provided by the referee. Support for this work was provided through NASA Contract NAS5-30612.

## REFERENCES

- Alpar, M. A. & Shaham, J. 1985, *Nature*, 316, 239
- Anders, E. & Ebihara, M. 1982, *Geochim. Cosmochim. Acta*, 46, 2363
- Asai, K., Dotani, T., Mitsuda, K., Nagase, F., Kamado, Y., Kuulkers, E., & Breedon, L. 1994, *PASJ*, 46, 479
- Brandt, W. N., Fabian, A., Dotani, T., Nagase, F., Inoue, H., & Kotani, T. 1996, *MNRAS*, 283, 1071
- Dower, R. G., Bradt, H. V., & Morgan, E. H. 1982, *ApJ*, 261, 228
- Goss, W. M. & Mebold, U. 1977, *MNRAS*, 181, 255
- Hasinger, G., van der Klis, M., Ebisawa, K., Dotani, T., & Mitsuda, K. 1990, *A&A*, 235, 131
- Hirano, A., Kitamoto, S., Yamada, T., Mineshige, Shin, & Fukue, J. 1995, *ApJ*, 446, 350
- Hoshi, R. & Mitsuda, K. 1991, *PASJ*, 43, 485
- Kaluźienski, L. J., Holt, S. S., Boldt, E. A., & Serlemitsos, P. J. 1976, *ApJ*, 208, L71
- Kuulkers, E., van der Klis, M., Oosterbroek, T., Asai, K., Dotani, T., van Paradijs, J., & Lewin, W. G. H. 1994, *A&A*, 289, 795
- Lamb, F. K., 1989 in *Proc. 23rd ESLAB Symp. on Two Topics in X-ray Astronomy*, ed. N. E. White (ESA SP-296) (Paris: ESA), 215
- Lamb, F. K., Shibazaki, N., Alpar, M. A., & Shaham, J. 1985, *Nature*, 317, 681
- Lamb, P. & Sanford, P. W. 1979, *MNRAS*, 188, 555
- Langmeier, A., Hasinger, G., & Trümper, J. 1990, *A&A*, 228, 89
- Lewin, W. H. G., Lubin, L. M., Tan, J., van der Klis, M., van Paradijs, J., Penninx, W., Dotani, T., & Mitsuda, K. 1992, *MNRAS*, 256, 545
- Makino, Y. 1993, Ph.D. thesis, Osaka University, Japan
- Makishima, K., Maejima, Y., Mitsuda, K., Bradt, H. V., Remillard, R. A., Tuohy, I. R., & Hoshi, R. 1986, *ApJ*, 308, 635
- Mitsuda, K. et al. 1984, *PASJ*, 36, 741
- Morgan, E. H., Remillard, R. A., & Greiner, J. 1997, *ApJ*, 482, 993
- Morrison, R. & McCammon, D. 1983, *ApJ*, 270, 119
- Murdin, P., Jauncey, D. L., Haynes, R. F., Lerche, I., Nicolson, G. D., Holt, S. S., & Kluzienski, L. J. 1980, *A&A*, 87, 292
- Oosterbroek, T., van der Klis, M., Kuulkers, E., van Paradijs, J., & Lewin, W. G. H. 1995, *A&A*, 297, 141
- Predehl, P. & Schmitt, J. H. M. M. 1995, *A&A*, 293, 889
- Psaltis, D., Lamb, F. K., & Miller, G. S. 1995, *ApJ*, 454, L137
- Psaltis, D. & Lamb, F. K. 1998, *Astrophysical and Astronomical Transactions*, in press
- Remillard, R. A., Morgan, E. H., McClintock, J. E., Bailyn, C. D., Orosz, J. A. 1998, *ApJ*, submitted
- Schulz, N. S., Hasinger, G., & Trümper, J. 1989 *A&A*, 225, 48
- Schulz, N. S. & Wijers, R.A.M.J. 1993 *A&A*, 273, 123
- Shirey, R. E., Bradt, H. V., Levine, A. M., & Morgan, E. H. 1996, *ApJ*, 469, L21 (Paper I)
- Shirey, R. E., Bradt, H. V., Levine, A. M., & Morgan, E. H. 1998, *ApJ*, 506, 374 (Paper II)
- Shirey, R. E., Levine, A. M., & Bradt, H. V. 1999, in preparation
- Shirey, R. E. 1998, Ph. D. Thesis, Massachusetts Institute of Technology
- Smale, A. P. 1998, *ApJ*, 498, L141
- Stewart, R. T., Nelson, G. J., Penninx, W., Kitamoto, S., Miyamoto, S., & Nicolson, G. D. 1991, *MNRAS*, 253, 212
- Tennant, A. F. 1987, *MNRAS*, 226, 971
- Tennant, A. F. 1988, *MNRAS*, 230, 403
- Tennant, A. F., Fabian, A. C., & Shafer, R. A. 1986b, *MNRAS*, 221, 27P
- van der Klis, M. 1994, *ApJS*, 92, 511

Vaughan, B. A., Van Der Klis, M., Wood, K. S., Norris, J. P., Hertz, P., Michelson, P. F., Van Paradijs, J. Lewin, W. H. G., Mitsuda, K., & Penninx, W. 1994, *ApJ*, 435, 362

White, N. E., Peacock, A., Hasinger, G., Mason, K. O., Manzo, G., Taylor, B. G., & Branduardi-Raymont, G. 1986, *MNRAS*, 218, 129

Zhang, W., Jahoda, K., Swank, J. H., Morgan, E. H., & Giles, A. B. 1995, *ApJ*, 449, 930

Zhang, W., Morgan, E. H., Jahoda, K., Swank, J. H., Strohmayer, T. E., Jernigan, G., & Klein, R. I. 1996, *ApJ*, 469, L29

Zhang, W., Strohmayer, T. E., & Swank, J. H. 1998, *ApJ*, 500, L167

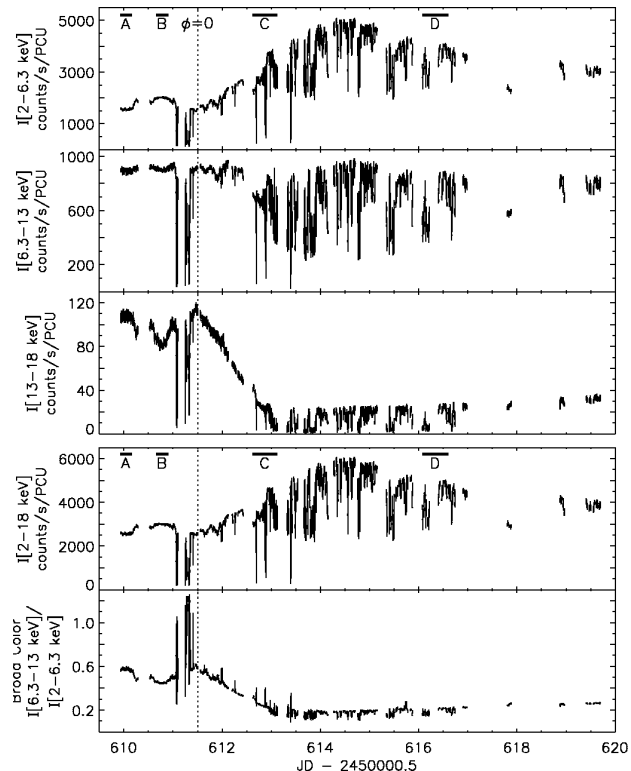


Fig. 1.— Light curves in three energy bands, the full 2–18 keV band, and a hardness ratio (broad color) for PCA observations of Cir X-1 from 1997 June 10–20, covering a 10-day period around phase zero ( $\phi = 0$ ; dashed line). JD 2450609.5 = 1997 June 10 0<sup>h</sup> UT. The intensities at the beginning of these observations (day 610) are typical “quiescent” levels. Each point represents 16 s of background-subtracted data from PCUs 0, 1, and 2. Segments labeled A, B, C, & D were used for spectral studies.

TABLE 1  
FIT PARAMETERS FOR SPECTRA A & B FOR FOUR MODELS.

$N_H/10^{22}$ ( $\text{cm}^{-2}$ )		Model Components <sup>a</sup>			Flux/ $10^{-8}$ <sup>b</sup> $\text{erg cm}^{-2} \text{s}^{-1}$	$\chi_r^2$ <sup>c</sup>
Self-Comptonized Bremsstrahlung						
		$kT$ (keV)	Optical depth	norm		
A	$2.80^{+0.22}_{-0.23}$	$2.78^{+0.04}_{-0.05}$	$11.05^{+0.47}_{-0.36}$	$4.54^{+0.24}_{-0.23}$	$2.73^{+0.02}_{-0.02}$	1.16–1.55
B	$3.94^{+0.18}_{-0.21}$	$2.89^{+0.12}_{-0.11}$	$7.20^{+0.71}_{-0.69}$	$9.67^{+0.37}_{-0.43}$	$3.04^{+0.02}_{-0.02}$	1.51–2.02
Blackbody						
		$kT$ (keV)	$R^d$ (km)	$kT$ (keV)	$R^d$ (km)	
A	$0.00^{+0.02}_{-0.00}$	$1.16^{+0.02}_{-0.02}$	$24.13^{+0.38}_{-0.37}$	$2.33^{+0.02}_{-0.03}$	$5.38^{+0.16}_{-0.15}$	$2.72^{+0.02}_{-0.02}$ 2.51–2.82
B	$0.01^{+0.21}_{-0.01}$	$1.12^{+0.01}_{-0.02}$	$30.46^{+0.92}_{-0.40}$	$2.20^{+0.03}_{-0.03}$	$5.59^{+0.27}_{-0.25}$	$3.04^{+0.02}_{-0.02}$ 1.42–1.78
Cutoff Power Law <sup>e</sup>						
		Photon index	$E_{cut}$ (keV)	norm	$kT$ (keV)	$R^d$ (km)
A	$0.27^{+0.94}_{-0.27}$	$-0.65^{+0.72}_{-0.30}$	$1.73^{+0.58}_{-0.24}$	$2.24^{+1.53}_{-0.47}$	$2.44^{+0.10}_{-0.05}$	$4.40^{+0.34}_{-0.87}$ $2.73^{+0.02}_{-0.02}$ 0.79–1.04
B	$1.95^{+0.74}_{-0.86}$	$-0.34^{+0.46}_{-0.60}$	$1.67^{+0.31}_{-0.27}$	$5.97^{+2.70}_{-2.29}$	$2.29^{+0.09}_{-0.07}$	$4.61^{+0.67}_{-0.73}$ $3.04^{+0.02}_{-0.02}$ 0.79–1.35
Disk Blackbody						
		$kT_{in}$ (keV)	$R_{in} \cos^{1/2} \theta^f$ (km)	$kT$ (keV)	$R^d$ (km)	
A	$1.44^{+0.26}_{-0.27}$	$1.81^{+0.08}_{-0.06}$	$9.39^{+0.64}_{-0.64}$	$2.47^{+0.04}_{-0.04}$	$4.10^{+0.25}_{-0.25}$	$2.73^{+0.02}_{-0.02}$ 0.79–1.06
B	$2.49^{+0.23}_{-0.23}$	$1.54^{+0.04}_{-0.04}$	$15.63^{+0.93}_{-0.84}$	$2.28^{+0.05}_{-0.05}$	$4.66^{+0.37}_{-0.37}$	$3.04^{+0.02}_{-0.02}$ 0.75–1.31

<sup>a</sup> Errors quoted are 90% confidence limits for a single parameter ( $\Delta\chi^2 = 2.7$ ).

<sup>b</sup>Total 2.5–25 keV flux.

<sup>c</sup>  $\chi^2/dof$ , where  $dof$  = the number of spectral bins (52–54 per spectrum) minus the number of fit parameters (4–6). The range of values represents the fits for the several PCU detectors.

<sup>d</sup>Blackbody radius for a distance of 8 kpc.

<sup>e</sup>Power law with exponential cut-off above  $E_{cut}$  (a Boltzmann-Wien spectrum).

<sup>f</sup> Inner radius of the accretion disk (times  $\cos^{1/2} \theta$ , where  $\theta$  is the angle between the normal to the disk and the line of sight) for a distance of 8 kpc.

TABLE 2  
FIT PARAMETERS FOR HID REGIONS 1–20 USING A MODEL CONSISTING OF A DISK BLACKBODY PLUS A  
BLACKBODY.

HID <sup>a</sup> region	$N_H/10^{22}$ ( $\text{cm}^{-2}$ )	$kT_{in}$ (keV)	$R_{in} \cos^{1/2} \theta$ <sup>b</sup> (km)	$kT$ (keV)	$R$ <sup>c</sup> (km)	Flux/ $10^{-8}$ <sup>d</sup> $\text{erg cm}^{-2} \text{s}^{-1}$	$\chi_r^2$ <sup>e</sup>
1	$1.83^{+0.28}_{-0.32}$	$1.45^{+0.05}_{-0.05}$	$19.29^{+1.31}_{-1.22}$	$2.16^{+0.09}_{-0.07}$	$3.65^{+0.50}_{-0.52}$	$2.89^{+0.03}_{-0.02}$	1.41–2.14
2	$1.97^{+0.30}_{-0.28}$	$1.41^{+0.04}_{-0.05}$	$20.87^{+1.46}_{-1.29}$	$2.15^{+0.09}_{-0.10}$	$3.71^{+0.68}_{-0.64}$	$2.99^{+0.02}_{-0.02}$	1.40–1.70
3	$2.04^{+0.27}_{-0.35}$	$1.38^{+0.04}_{-0.04}$	$22.24^{+1.30}_{-1.16}$	$2.08^{+0.09}_{-0.08}$	$4.00^{+0.56}_{-0.52}$	$2.96^{+0.02}_{-0.02}$	1.32–1.81
4	$2.18^{+0.37}_{-0.32}$	$1.36^{+0.05}_{-0.06}$	$23.46^{+2.27}_{-1.85}$	$2.07^{+0.18}_{-0.17}$	$3.89^{+1.27}_{-1.18}$	$3.02^{+0.03}_{-0.02}$	2.21–3.47
5	$2.29^{+0.33}_{-0.27}$	$1.31^{+0.03}_{-0.05}$	$27.22^{+1.97}_{-1.74}$	$2.02^{+0.11}_{-0.14}$	$3.78^{+0.97}_{-0.94}$	$3.21^{+0.02}_{-0.02}$	2.51–3.24
6	$2.35^{+0.30}_{-0.24}$	$1.34^{+0.03}_{-0.04}$	$26.21^{+1.33}_{-1.19}$	$2.02^{+0.11}_{-0.13}$	$3.31^{+0.58}_{-0.53}$	$3.37^{+0.02}_{-0.02}$	1.41–1.55
7	$2.31^{+0.24}_{-0.25}$	$1.30^{+0.02}_{-0.03}$	$28.67^{+1.20}_{-1.05}$	$2.03^{+0.09}_{-0.11}$	$3.30^{+0.65}_{-0.57}$	$3.27^{+0.02}_{-0.02}$	2.22–2.76
8	$2.27^{+0.29}_{-0.25}$	$1.29^{+0.02}_{-0.03}$	$30.06^{+1.70}_{-1.48}$	$2.01^{+0.12}_{-0.14}$	$3.34^{+0.91}_{-0.83}$	$3.46^{+0.03}_{-0.02}$	2.41–2.70
9	$2.18^{+0.21}_{-0.24}$	$1.30^{+0.03}_{-0.03}$	$30.68^{+1.15}_{-1.07}$	$2.01^{+0.14}_{-0.14}$	$3.36^{+0.85}_{-0.69}$	$3.75^{+0.02}_{-0.02}$	2.29–2.44
10	$2.01^{+0.23}_{-0.24}$	$1.31^{+0.02}_{-0.02}$	$31.35^{+1.31}_{-1.10}$	$2.01^{+0.12}_{-0.11}$	$3.02^{+0.86}_{-0.67}$	$4.15^{+0.02}_{-0.03}$	1.82–2.56
11	$1.98^{+0.19}_{-0.22}$	$1.30^{+0.02}_{-0.02}$	$32.90^{+1.24}_{-1.17}$	$1.93^{+0.08}_{-0.08}$	$3.52^{+0.67}_{-0.54}$	$4.39^{+0.03}_{-0.03}$	2.55–3.05
12	$1.78^{+0.22}_{-0.26}$	$1.29^{+0.02}_{-0.02}$	$33.41^{+1.51}_{-1.34}$	$1.94^{+0.17}_{-0.12}$	$3.09^{+0.82}_{-0.72}$	$4.35^{+0.03}_{-0.03}$	2.87–3.06
13	$1.63^{+0.21}_{-0.25}$	$1.28^{+0.02}_{-0.02}$	$34.02^{+1.09}_{-0.92}$	$2.12^{+0.22}_{-0.19}$	$1.51^{+0.70}_{-0.47}$	$4.21^{+0.03}_{-0.03}$	3.74–4.66
14	$1.53^{+0.18}_{-0.17}$	$1.26^{+0.01}_{-0.02}$	$33.94^{+1.28}_{-1.06}$	$2.34^{+0.53}_{-0.40}$	$0.84^{+0.77}_{-0.46}$	$3.98^{+0.03}_{-0.03}$	4.19–5.11
15	$1.48^{+0.15}_{-0.16}$	$1.22^{+0.01}_{-0.01}$	$35.30^{+0.51}_{-0.49}$	...	...	$3.68^{+0.02}_{-0.02}$	5.15–6.34
16	$1.43^{+0.19}_{-0.17}$	$1.19^{+0.01}_{-0.01}$	$35.88^{+0.50}_{-0.48}$	...	...	$3.32^{+0.02}_{-0.02}$	5.91–7.52
17	$0.94^{+0.17}_{-0.15}$	$1.20^{+0.01}_{-0.01}$	$32.69^{+0.23}_{-0.53}$	...	...	$3.00^{+0.02}_{-0.01}$	5.87–7.16
18	$0.56^{+0.16}_{-0.18}$	$1.26^{+0.01}_{-0.01}$	$28.22^{+0.49}_{-0.48}$	...	...	$2.94^{+0.02}_{-0.02}$	9.59–11.39
19	$0.64^{+0.17}_{-0.16}$	$1.29^{+0.01}_{-0.01}$	$27.02^{+0.35}_{-0.36}$	...	...	$3.08^{+0.02}_{-0.02}$	9.36–10.45
20	$0.81^{+0.15}_{-0.19}$	$1.33^{+0.01}_{-0.01}$	$26.25^{+0.38}_{-0.37}$	...	...	$3.24^{+0.02}_{-0.02}$	14.67–17.01

<sup>a</sup> Errors quoted are 90% confidence limits for a single parameter ( $\Delta\chi^2 = 2.7$ ).

<sup>b</sup> Inner radius of the accretion disk (times  $\cos^{1/2} \theta$ , where  $\theta$  is the angle between the normal to the disk and the line of sight) for a distance of 8 kpc.

<sup>c</sup> Blackbody radius for a distance of 8 kpc.

<sup>d</sup> Total 2.5–25 keV flux.

<sup>e</sup>  $\chi^2/dof$ , where  $dof$  = the number of spectral bins (52–54 per spectrum) minus the number of fit parameters (3–5). The range of values represents the fits for the several PCU detectors.

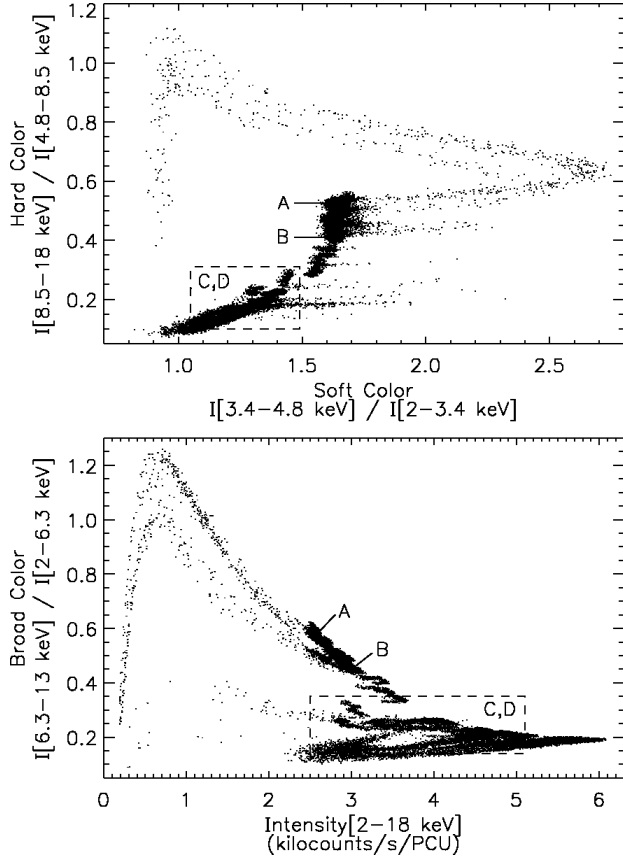


Fig. 2.— Color-color and hardness-intensity diagrams from PCA observations during 1997 June 10–20 (the entire period covered by Fig. 1). Each point represents 16 s of background-subtracted data from PCUs 0, 1, and 2. Time segments A & B, defined in Fig. 1, produced small clusters whose locations are indicated in the diagrams. Time segments C & D produced extended tracks within the dashed boxes, which define the plot ranges of Fig. 3

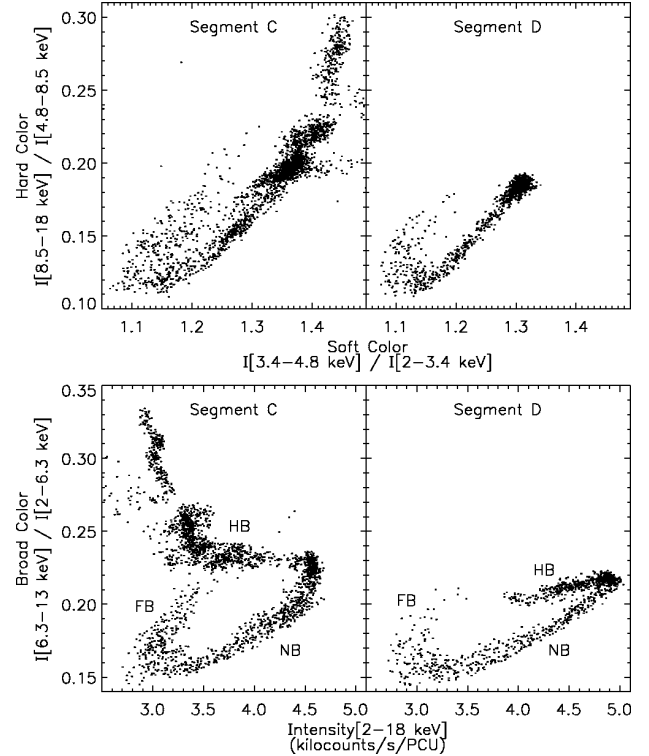


Fig. 3.— Color-color and hardness-intensity diagrams from time segments C (left panels) and D (right panels) of Fig. 1. In the HID, horizontal, normal, and flaring branches (HB/NB/FB) have been identified. Each point represents 16 s of background-subtracted data from PCUs 0, 1, and 2. The ranges of these diagrams are indicated in Fig. 2 by dashed boxes.

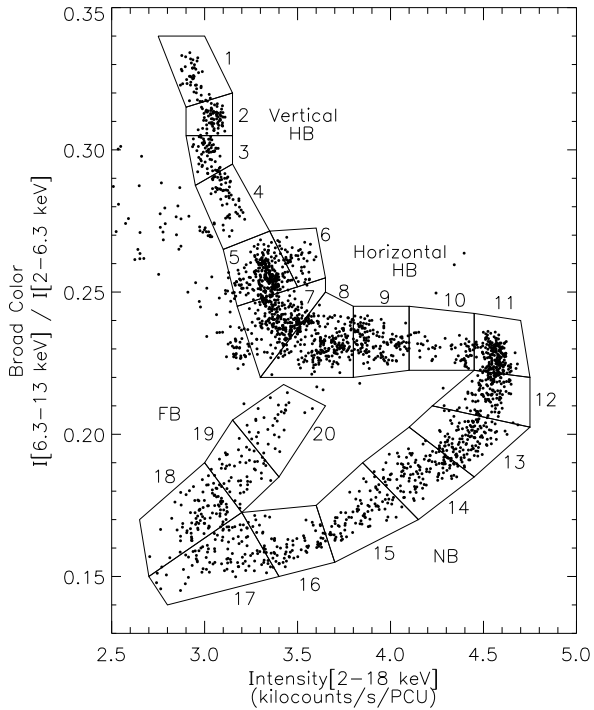


Fig. 4.— Hardness-intensity diagram from time segment C. The HID track has been divided into 20 regions which were used to group data for construction of average power density spectra and energy spectra.

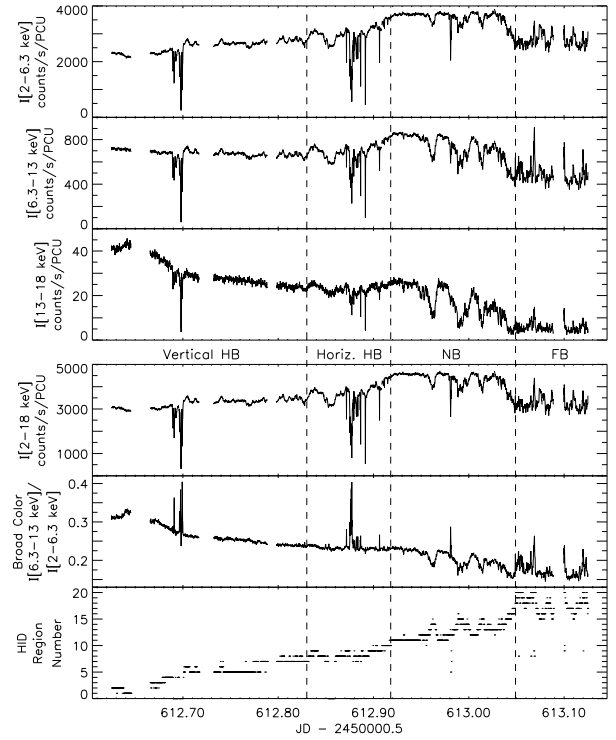


Fig. 5.— Top: expanded light curves in 3 energy channels, and bottom: total 2–18 keV light curve, broad color, and HID regions for time segment C. The predominant spectral branch is identified for each portion of the data, based on HID region numbers. Absorption dips (omitted from HID regions) are clearly identified by decreased intensity coupled with pronounced increases in broad-color.

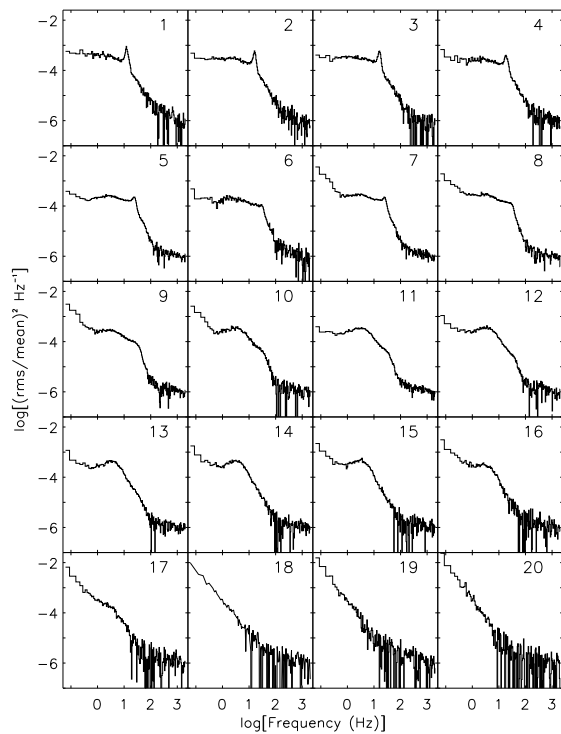


Fig. 6.— Averaged and rebinned Fourier power density spectra (2–32 keV) for each of the 20 regions along the HID track in Fig. 4. The estimated Poisson noise level has been subtracted from each PDS.

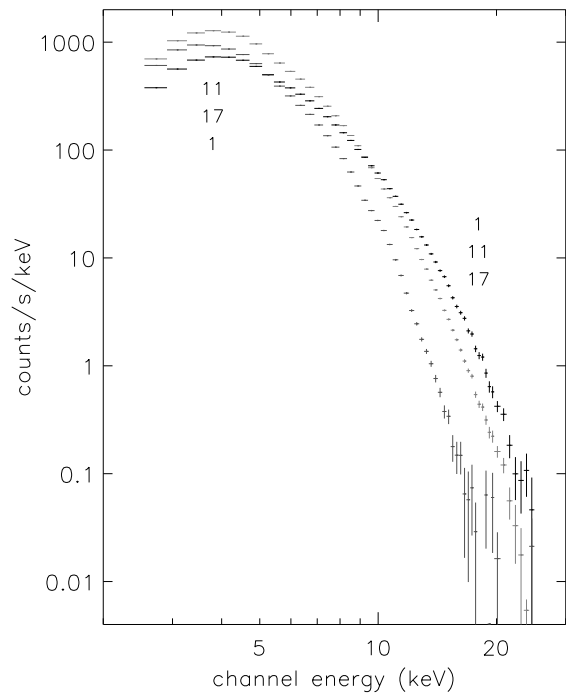


Fig. 7.— Pulse-height spectra (2.5–25 keV; PCU 0 only) from the hard, bright, and soft extremes, regions 1, 11, and 17 respectively, of the HID track in Fig. 4. Labels for the region numbers are ordered vertically to match the relative intensities at the low and high-energy ends of the spectra.



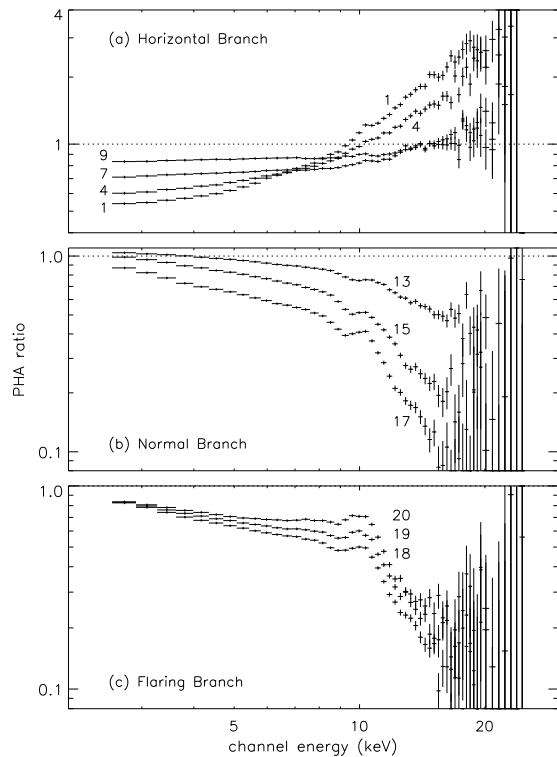


Fig. 8.— Ratio of pulse-height spectra (PCU 0 only) from selected HID regions to the pulse-height spectrum of Region 11, showing the evolution of the spectrum along the (a) horizontal, (b) normal, and (c) flaring branches.

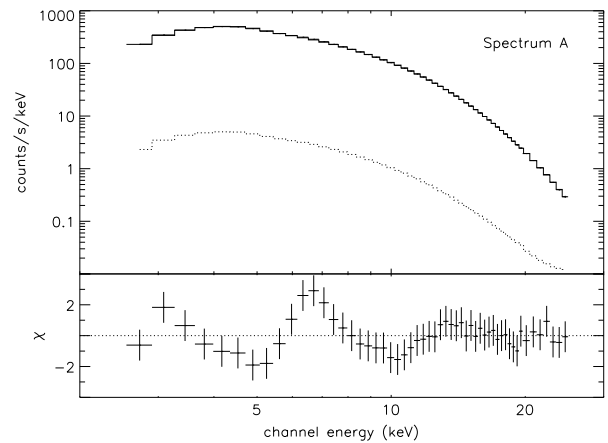


Fig. 9.— Spectrum A and model (histogram) consisting of a disk blackbody and blackbody (see Table 1). The  $1\text{-}\sigma$  uncertainty, shown in the top panel as a dotted curve below the spectrum, is dominated by the 1% systematic error for all channels below  $\sim 20$  keV. The residuals ( $\chi$ ), divided by the  $1\sigma$  uncertainty, show a peak at 6–7 keV that may be due to an iron emission line.

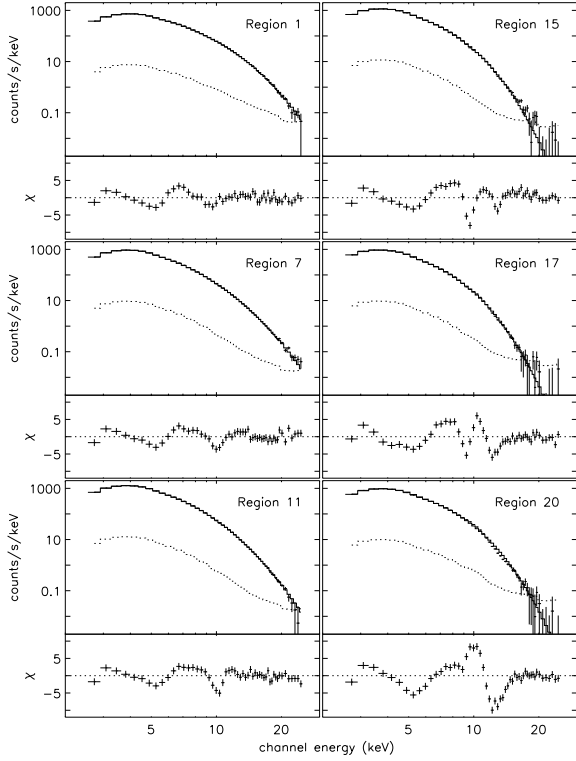


Fig. 10.— Fitted pulse-height spectra and residuals ( $\chi$ ) for selected HID regions (PCU 0 only). The  $1\text{-}\sigma$  uncertainties for each spectrum, shown as dotted curves below the spectra, are dominated by the 1% systematic error for all channels below  $\sim 10$  keV. Fit parameters are listed in Table 2. Towards higher region number, the residuals show an unusual line- or edge-like feature near 10 keV.

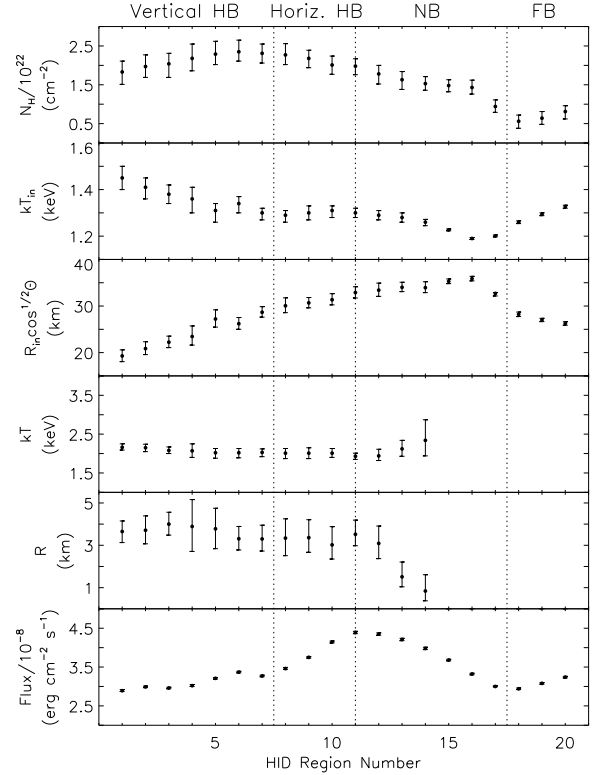


Fig. 11.— Spectral fit parameters for the disk blackbody plus blackbody model versus HID region number. The plot is divided by vertical dotted lines into four parts corresponding to branches of the HID track.

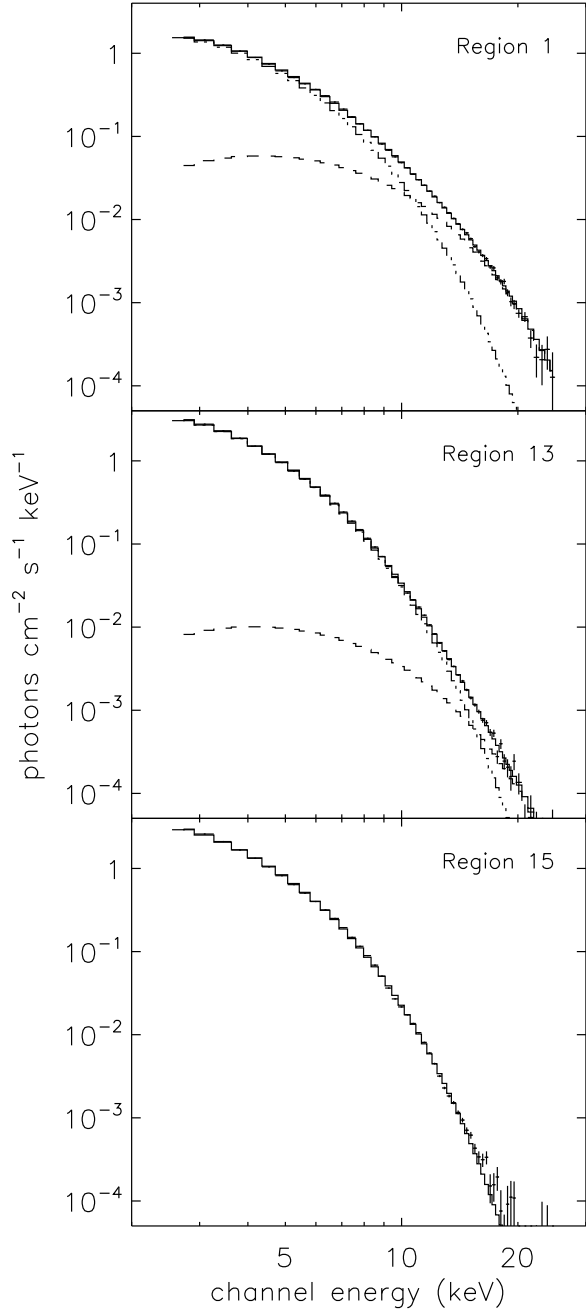


Fig. 12.— Modeled incident spectra for HID regions 1, 13, and 15, showing the two components (disk blackbody and blackbody) and the sum. The disk blackbody dominates at low energy, and the blackbody generally dominates at high energy but has faded away entirely in region 15. The data shown are for PCU 0 only. Fit parameters are listed in Table 2.

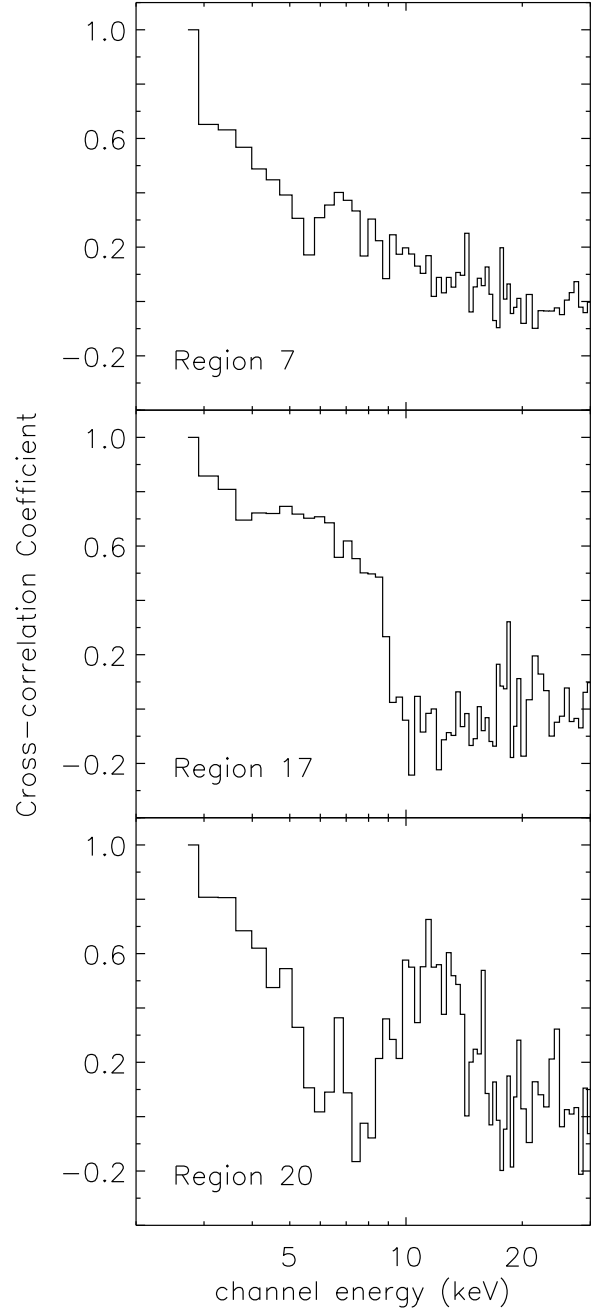


Fig. 13.— Linear cross-correlation coefficients of time-series data (16 s bins) in each energy channel to that of the lowest-energy channel for HID regions 7, 17, and 20. Towards higher region number, a step or peak develops in the cross-correlation coefficient near 10 keV and may be related to the feature seen at similar energy in the corresponding pulse-height spectra and PHA ratios.